Soaking in CO₂ Huff-n-Puff: A Single-Nanopore Scale Study

Do Yoon Moh, ¹ Hongwei Zhang, ¹ Shihao Wang, ² Xiaolong Yin, ³ and Rui Qiao^{1,*}

Abstract. CO₂ Huff-n-Puff is a promising method for enhancing the oil recovery from unconventional reservoirs and sequestering CO₂. Optimizing the operation of Huff-n-Puff requires a fundamental understanding of the thermodynamic and transport phenomena of CO₂ and oil in nanopores. Here, we investigate the soaking step of CO₂ Huff-n-Puff in a single, 4 nm-wide calcite pore using molecular dynamics simulations. We show that the CO₂ molecules entering the pore can become adsorbed on pore walls and diffuse along with walls or are transported into the pore's interior as free CO₂ molecules. Decane molecules are displaced from the pore walls and out of the bulk zone in the pore. Before reaching the pore's end, the movement of the density fronts of adsorbed and free CO₂ molecules inside the pore obeys a $t^{1/2}$ scaling law with effective diffusion coefficients ~50% smaller than that of bulk CO₂. Except at the very beginning period of soaking, the accumulation of adsorbed and free CO₂ molecules occurs at a similar rate and follows the diffusive scaling law. These pore-scale results highlight the importance of surface adsorption on the storage and transport of CO₂ during the soaking process in unconventional oil reservoirs.

¹ Department of Mechanical Engineering, Virginia Tech, Blacksburg, VA 24061, USA ² Chevron Energy Technology Co., 1500 Louisiana Street, Houston, TX 77002, USA

³ Petroleum Engineering Department, Colorado School of Mines, Golden, CO 80401, USA

^{*} Corresponding author. Email: ruiqiao@vt.edu.

1. Introduction

21

22

23

24

25

26

27

28

29

30

31

32

33

34

35

36

37

38

39

40

41

42

43

in the US over the last decade. In these unconventional reservoirs, oil is trapped in rocks featuring pervasive nanopores, and the low permeability of these rocks makes oil recovery challenging.² The recovery rate of these reservoirs is typically 1 to 7%, much lower than conventional reservoirs. Because of unconventional reservoirs' low permeability and poor injectability, conventional improved and enhanced oil recovery methods based on water or gas flooding cannot be applied. Enhanced oil recovery (EOR) instead needs to operate on the principle of injection and extraction through the Huff-n-Puff scheme.^{3, 4} Huff-n-Puff utilizes a single well and includes three steps. In the "Huff" step, a gas is injected into the reservoir through a well. Next, in the soaking step, the well is shut for an extended period of time. Finally, in the "Puff" step, the well is open to produce gas and oil. Gases capable of extracting oil, such as CO2, methane, and methane enriched with ethane / propane, can all be used. When CO₂ is used, Huff-n-Puff is not only effective as an EOR technique⁵ but also offers an additional benefit of CO₂ storage because part of the injected CO₂ does not return to the surface. When a reservoir's oil production becomes marginally economical, CO₂ Huff-n-Puff could receive credits from CO₂ sequestration. CO₂ sequestration in unconventional oil reservoirs has been successfully tested in recent field studies. While CO₂ Huff-n-Puff for EOR and CO₂ sequestration in unconventional oil reservoirs have shown promise, many challenges remain.^{4, 6-9} Indeed, limited or no EOR was observed in some CO₂ Huff-n-Puff field tests. ¹⁰ These poor results are partly caused by the fact that the success of Huff-n-Puff requires a large number of parameters (e.g., duration of gas injection and soaking) to be optimized simultaneously. 11 Meanwhile, the selection of unconventional reservoirs suitable for CO₂ sequestration lacks practical guidelines. Addressing these challenges requires a fundamental

Shale and tight oil reservoirs have become a significant source of petroleum liquid production

understanding of the thermodynamic and transport behavior of oil and CO₂ in unconventional reservoirs.

Much research has been devoted to these topics in recent years, e.g., properties such as CO₂ solubility and diffusivity, oil swelling factor, and oil-CO₂ miscibility have been studied as functions of temperature and pressure and correlated to oil production rate.^{3, 4, 12-16} These works laid the foundation for physics-based simulation of EOR and CO₂ storage in unconventional reservoirs. In particular, numerical modeling of the Huff-n-Puff process has provided significant insight into the many tradeoffs that must be balanced. An emerging picture from these studies is that oil and CO₂ in these reservoirs cannot always be treated as bulk fluids, which are usually deemed adequate in conventional reservoirs.¹⁷

In unconventional reservoirs, the surface-to-volume ratio is large because of the prevalence of nanopores. Therefore, interactions between CO₂ and oil molecules with pore walls can potentially affect their behaviors in unconventional reservoirs. For example, oil and CO₂ can exhibit critical properties and phase behavior different from their bulk counterparts. ¹⁸⁻²⁰ Both pore size and its distribution affect the behavior of fluid mixtures in unconventional reservoirs. ²¹⁻²⁴ For inorganic pores, strong adsorption of CO₂ can occur on their walls due to the strong affinity of CO₂ to pore walls, ²⁵⁻²⁸ while oil molecules with relatively weaker affinity to pore walls than CO₂ molecules are displaced from pore walls. Depending on the adsorption density of CO₂ on pore walls, both enhancement of oil flow²⁸⁻³⁰ and retardation of oil flow can occur. ²⁸ Furthermore, the interactions between CO₂ and pore walls, pore size, and the solubility of CO₂ in oil in presence of co-solvents were found to affect the oil recovery rate from nanopores. ^{22, 24} These previous works highlight the importance of thermodynamic and transport phenomena at the nanopore scale in determining the oil production and CO₂ sequestration at the macroscopic scale.

In this work, we investigate the soaking step of CO₂ Huff-n-Puff at the single-nanopore scale. Pore-scale research on this topic is scarce³¹, and many questions remain open. For example, how do CO₂ molecules move into nanopores? Does the accumulation of CO₂ and depletion of oil follow any scaling law? How do pore walls affect the transport of CO₂ molecules into nanopores and their accumulation inside pores? To answer these questions, we perform non-equilibrium molecular dynamics (MD) simulations to obtain a molecular picture of CO₂ and oil transport during soaking. To gain insights into the observed phenomena, we also perform auxiliary equilibrium simulations to probe the thermodynamics and dynamics of CO₂ molecules at oil-wall interfaces.

2. Simulation Systems, Molecular Models, and Methods

Simulation systems and protocol. Figure 1a shows a schematic of the MD system designed to study the soaking process of CO₂ Huff-n-Puff. The system includes two main parts: a slit-shaped calcite nanopore and a "reservoir." The pore represents a dead-end pore in oil shales, and the "reservoir" mimics the microfracture or macropore to which the pore is connected. A calcite pore is adopted because a significant amount of oil can be stored in inorganic pores (e.g., in the chalks of the Niobrara petroleum system, calcite is the dominant mineral, kerogen is scarce, and oil is trapped mainly in inorganic pores). The center-to-center width of the pore, w, is 4.0 nm. The length of the pore, L_p , is set to 29.504 nm. This pore is slender enough ($L_p/w \approx 7.4$) for studying the transport of oil and CO₂ along the pore, yet it is not too long, so the computational cost is not prohibitively high. The system is periodic in all three directions, and the simulation box measures 90 nm, 2.928 nm, and 13.306 nm, in the x-, y-, and z- directions, respectively.

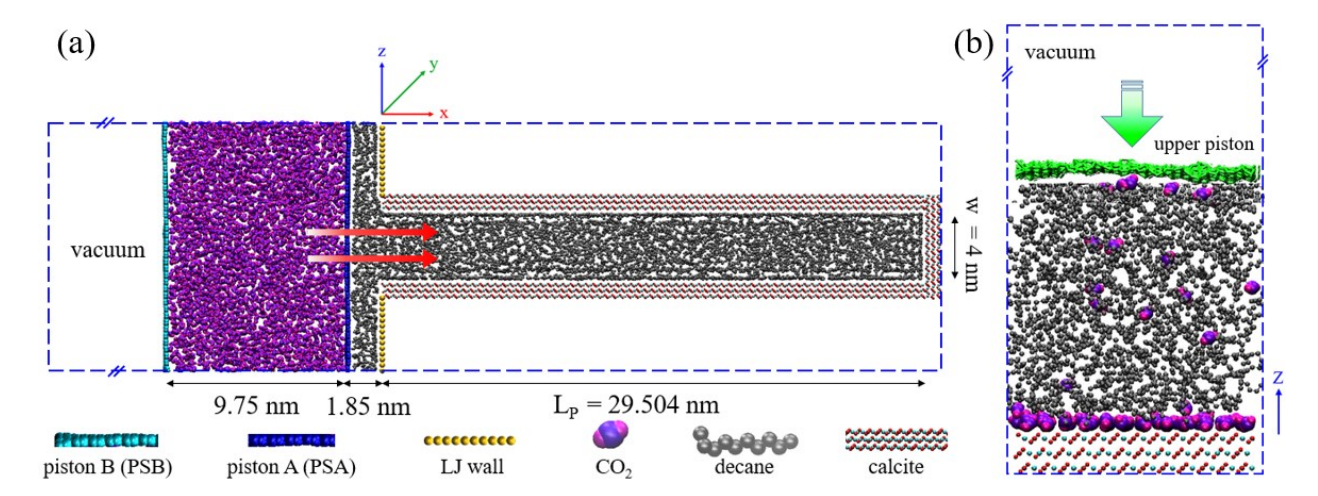


Figure 1. Schematics of simulation systems for studying the soaking process in a single calcite slit nanopore connected to a reservoir (a) and the properties of CO_2 at oil-calcite interfaces (b). In (a), x = 0 corresponds to the pore entrance, and z = 0 corresponds to the lower calcite wall's uppermost oxygen atom layer. In (b), z = 0 corresponds to the lower calcite wall's uppermost oxygen atom layer. The dashed blue lines denote the simulation box.

To study the soaking process, we set up the initial distributions of oil (taken as decane here) and CO₂ in the system via two successive steps to mimic the state of oil and CO₂ at the end of a Huff step. In the first step, only decane molecules are packed into the pore and a small portion of the reservoir using the Packmol code.³⁵ The pressure of the decane is adjusted to 280 bar using piston A in Fig. 1a. The system is equilibrated for 5 ns. Piston A is then fixed. A short equilibrium run is conducted, during which the decane pressure is obtained by calculating the force per unit area on piston A. The result agrees with 280 bar very well. In the second step, piston A is fixed, and CO₂ molecules are packed into the reservoir (between pistons A and B in Fig. 1a). The pressure of CO₂ is adjusted to 410 bar using piston B, and the system is equilibrated for 10 ns. Piston B is then fixed and the CO₂ pressure is verified using the process described above for the decane pressure. There are 1128 and 4000 decane and CO₂ molecules in the system at the end of these steps, respectively. Note that the number of CO₂ molecules is tuned empirically so that, for a pressure of 280 bar on piston A, the pore is filled fully by decane and a thin decane layer (~1.85 nm) exists next to the pore in reservoir. The number of CO₂ molecules is tuned to ensure that, at

an initial CO₂ pressure of 410 bar, the volume occupied by CO₂ is sufficiently large. The piston A and B are located at 1.85 and 11.59 nm from the pore entrance, respectively. At last, piston A is removed and piston B is fixed (this time instant is defined as t=0), and the system is simulated for 45 ns. This "soaking" simulation mimics the soaking step of the CO₂ Huff-n-Puff operations, during which the well is shut and thus the system volume is fixed. The pressure of the fluids in the reservoir is monitored by computing the force acting on piston B. To improve the MD statistics, two additional simulations with independent initial configurations are performed and the results shown here are the average of the three simulations. This simulation is hereafter referred to as the soaking simulation. The evolution of decane and CO₂ density distributions inside the pore is recorded on the fly during this simulation.

Because of the prominent role of interfacial CO₂ in the soaking process, we also build separate MD systems to study the properties of CO₂ molecules at calcite-decane interfaces. As shown in Fig. 1b, these systems feature a slab of decane and CO₂ mixture positioned on a calcite wall. The calcite wall and the simulation box both measure $4.846 \times 3.984 \text{ nm}^2$ in the *xy*-plane. The simulation box is 20 nm long in the *z*-direction. The pressure of the mixture is kept at 220 or 320 bar using a piston. These pressures are close to the CO₂-oil pressure at the beginning and final stages of the soaking simulations (see below). The number of CO₂ molecules is varied from 4 to 350 in different simulations to produce different adsorption densities of CO₂ on the calcite wall. The number of decane molecules is 360 in all simulations. After the desired number of decane and CO₂ molecules are packed between the calcite wall and the piston, equilibrium simulations (typically 55 ns) are performed to study the adsorption and dynamics of CO₂ molecules. The equilibrium thickness of the decane-CO₂ slab is 6.12 to 7.04 nm in these simulations, which is large enough to ensure that the middle portion of the slab is bulk-like.

Molecular models. The calcite walls are cut from a calcite crystal in the [1014] direction, and their atoms are fixed throughout all simulations. To reduce the computational cost, the thickness of the calcite wall is 0.91 and 1.82 nm in the systems shown in Fig. 1a and 1b, respectively. The Lennar-Jones (LJ) parameters and partial charges of calcite atoms are taken from the re-fitted Dove's potential. The vertical walls near the pore entrance in Fig. 1a are made of a sheet of LJ atoms arranged in a square lattice (lattice spacing: 0.3 nm). Both piston A and piston B are made of LJ atoms. Decane is modeled using the NERD force fields. The core fields developed by Zhu *et al.* The interactions between decane and CO₂ are described using the LJ potential using the parameters optimized by Wang et al. CO₂ and decane to be modeled accurately. For example, simulations based on these force fields can predict the solubility of CO₂ in decane at a temperature of 344.3 K and pressure up to 100 bar accurately. The LJ parameters for non-electrostatic interactions between other dissimilar atoms are obtained using the Lorentz-Berthelot combination rule.

Simulation methods. Simulations are performed using a customized GROMACS 4.5.6 code in the NVT ensemble. The temperature of decane and CO₂ is kept at 345 K in all simulations using the velocity rescaling thermostat with a time constant of 1 ps. A time step of 2 fs is used for equilibration. A time step of 1 fs is used for non-equilibrium simulations of soaking shown in Fig. 1a and the production run of CO₂-decane-calcite systems shown in Fig. 1b. LJ potentials are computed using direct summation, and electrostatic interactions are computed using the Particle mesh Ewald (PME) method with an FFT spacing of 0.12 nm. A cut-off length of 1.2 nm is used for both LJ potential and the real-space part of electrostatic interactions. For systems shown in Fig. 1b, a slab correction is applied. This correction, along with the large vacuum space left above the

piston, effectively removes the periodicity in the z-direction.

3. Results and Discussion

154

155

156

157

158

159

160

161

162

163

164

165

166

167

168

169

170

171

172

173

174

175

3.1 CO₂ at calcite-decane interfaces

Previous studies showed that CO₂ can adsorb strongly on mineral surfaces, with the adsorption on calcite surfaces easily reaches full monolayer coverage. 25-28 This adsorption can affect the storage and transport of decane/CO₂ in inorganic nanopores and thus should affect the soaking process. Therefore, to help understand the results of soaking simulations, we first examine the adsorption of CO₂ at calcite-decane interfaces and the dynamic properties of interfacial CO₂ molecules using the MD system shown in Fig. 1b. Figure 2a shows the CO₂ and decane density profiles near a calcite surface exposed to a decane-CO₂ mixture in a representative case where the bulk CO₂ density is $\rho_{co2}^b = 0.61 \text{ nm}^{-3}$ (profiles for other cases are shown in Fig. S1 in the Supplementary Material) and the mixture pressure is 320 bar. Near the calcite surface, several layers of decane molecules are identified, as has been widely observed.^{25, 26} A significant enrichment of CO₂ molecules occurs near the calcite surface. In particular, a distinct layer corresponds to the CO₂ molecules in contact with the calcite surface is observed in the region 0 nm < z < 0.398 nm. This accumulation of interfacial CO₂ is driven by the quadruple-charge interactions between CO₂ molecules and calcite surface atoms. Hereafter, CO₂ molecules in this layer are referred to as "adsorbed" CO2. The density of adsorbed CO2 on the calcite surface is computed using $\Gamma_{co2} = \int_0^{0.398 \, \mathrm{nm}} \rho_{co2}(z) dz$. Figure 2b shows the adsorption isotherms of CO₂ on calcite surface as a function of bulk CO₂ density. High adsorption density is observed at even very low bulk CO₂ densities, consistent with the strong affinity of CO₂ molecules

to calcite. 25, 26 As bulk CO₂ density increases, Γ_{co2} approaches an asymptotic value of Γ_{co2}^{∞} =

5.15 nm⁻², when the calcite surface is fully covered by CO₂ molecules. The adsorption isotherm is little changed as the pressure of decane-CO₂ mixtures changes from 320 to 220 bar (the CO₂ adsorption isotherm at 220 bar is shown in Fig. S2), suggesting that CO₂ adsorption and the concurrent displacement of decane molecules from CO₂ adsorption site is controlled primarily by CO₂-calcite interactions.

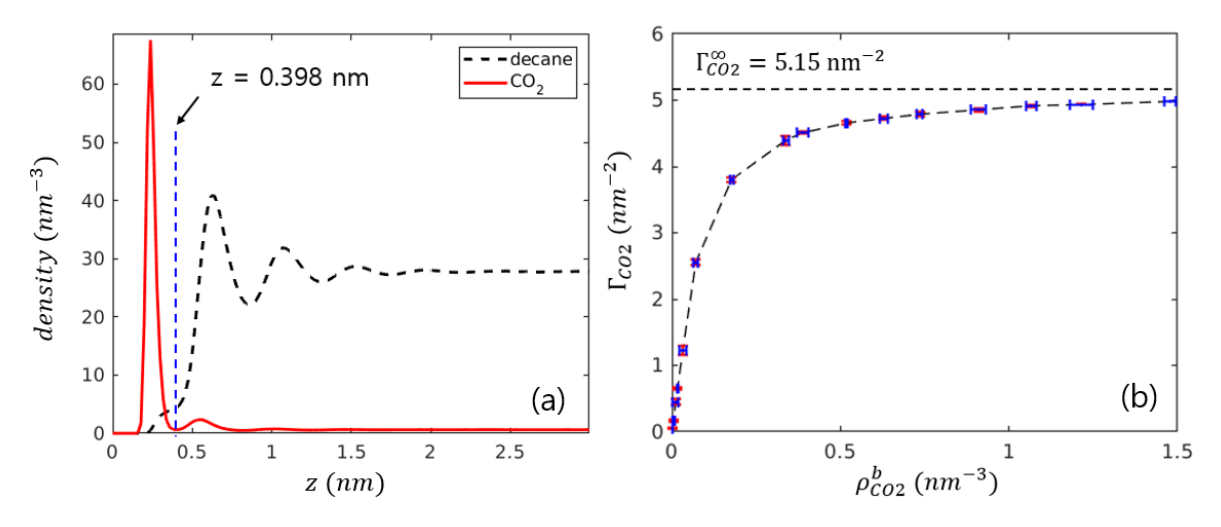


Figure 2. (a) Density profiles of decane and CO₂ near a calcite surface when the bulk CO₂ density is $\rho_{co2}^b = 0.61 \text{ nm}^{-3}$. (b) Adsorption isotherm of CO₂ at the calcite-decane interface. The pressure of the decane-CO₂ mixture is 320 bar.

We next characterize the dynamics of adsorbed and bulk CO₂ molecules. To compute the diffusion coefficient of adsorbed CO₂ molecules, in each trajectory frame of the simulation performed for the system shown in Fig. 1b, we identify the CO₂ molecules adsorbed on the calcite wall first. We then compute the mean-square-displacement (MSD) of these molecules for 8 ps. This process is repeated for each frame in the trajectory to obtain an ensemble average of the MSD of the adsorbed CO₂ molecules, from which the diffusion coefficient is computed. Because of the exchange between adsorbed and bulk CO₂, an adsorbed CO₂ molecule can become bulk CO₂ when its MSD is being evaluated (i.e. within 8 ps). Such kind of event, however, is rare since the exchange occurs at a nanosecond time scale (see below). The diffusion coefficient of bulk CO₂ is evaluated similarly.

Figure 3 shows the self-diffusion coefficient of the CO₂ molecules in bulk decane-CO₂ mixture and adsorbed on calcite surfaces. We observe that, as the bulk mixture's pressure increases from 220 bar to 320 bar, the diffusion coefficient decreases modestly. As bulk CO₂ density increases, Fig. 3a shows that CO₂ molecules' diffusion coefficient in bulk increases modestly. This is expected because, as the CO₂ mole fraction increases, decane-CO₂ mixtures become less viscous, and it follows from the Einstein relation that the diffusion of small CO₂ molecules in these fluid mixtures should increase. On the other hand, Fig. 3b shows that the lateral diffusion coefficient of CO₂ molecules adsorbed on calcite surfaces decreases by about 60% as the adsorption density increases from zero to near saturation. Such a slowdown of diffusion is expected. The diffusion of a CO₂ molecule on the calcite surface studied here involves the displacement of adsorbed decane and CO₂ molecules adjacent to it. Since the adsorption of CO₂ molecules is stronger than that of decane molecules, diffusion of adsorbed CO₂ molecules becomes more difficult as more adsorbed decane molecules are replaced by CO₂ molecules. Overall, the diffusion of CO₂ molecules adsorbed on a calcite surface is 12-30 times slower than in bulk decane-CO₂ mixtures.

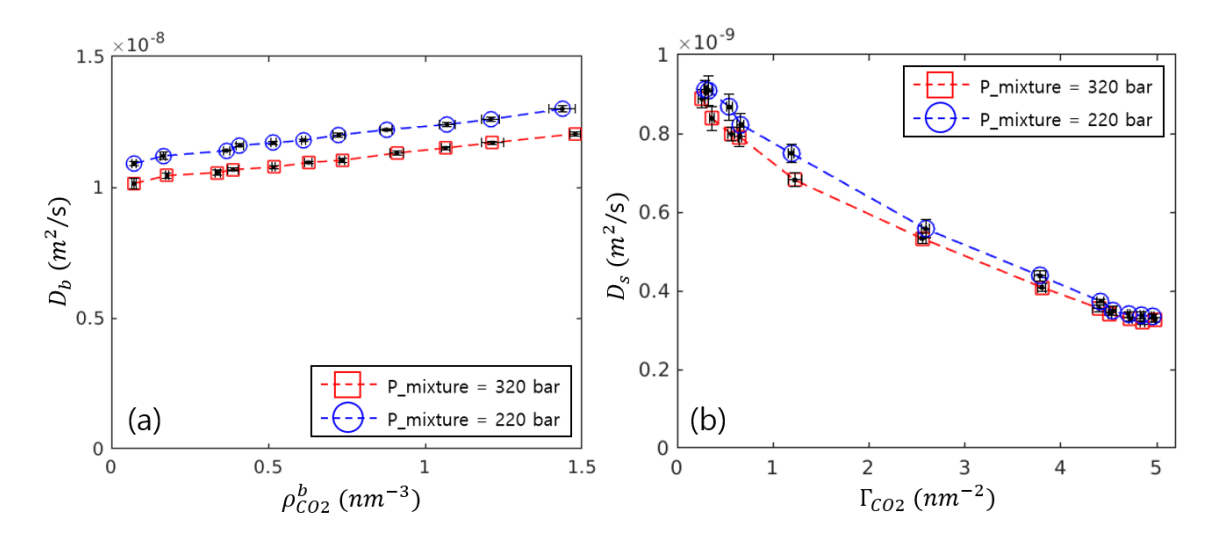


Figure 3. Self-diffusion coefficient of CO_2 molecules in bulk decane- CO_2 mixtures (a) and adsorbed on calcite surface (b) at a pressure of 220 and 320 bar. In (b), the lateral diffusion coefficient is shown.

CO₂ molecules adsorbed on a calcite surface can leave the surface, which is also manifested as the exchange between adsorbed CO₂ molecules and CO₂ molecules unassociated with the surface which is hereafter termed as "free" CO₂ (z > 0.398 nm). To quantify such an exchange, we compute the residence auto-correlation function for CO₂ molecules adsorbed on calcite surfaces²⁶

216
$$C_R(t) = \frac{\langle p(0)p(t)\rangle}{\langle p(0)p(0)\rangle} \tag{1}$$

212

213

214

215

217

218

219

220

221

222

223

224

225

226

227

228

229

230

231

where p(t) = 1 if a CO₂ molecule resides in the adsorption zone $(0 \le z \le 0.398 \text{ nm})$ at t = 0 is also found in that zone at time t. $\langle \cdots \rangle$ denotes the ensemble average. The correlation function $C_R(t)$ decays rapidly to zero if the adsorbed CO₂ molecules exchange rapidly with the free CO₂ molecules. The time scale of decay estimates the residence time of an adsorbed CO2 molecule on the calcite surface. Figure 4 shows $C_R(t)$ for different CO₂ adsorption densities when the pressure of the decane-CO₂ mixture is 320 bar (those for the pressure of 220 bar are very similar and shown in Fig. S3). The exchange between adsorbed and free CO2 molecules becomes more facile as the adsorption density increases. However, even at an adsorption density of 0.256 nm⁻², $C_R(t)$ decreases to 0.3 within 4 ns. These results suggest that, despite the strong affinity of CO₂ molecules to calcite surfaces, adsorbed CO2 molecules can become desorbed and exchange with free CO2 molecules in the bulk decane-CO₂ mixture at a nanosecond time scale. The nanosecond time scale exchange between adsorbed and free CO₂ molecules has been observed by Wang et al.²⁶ The exchange revealed here is somewhat slower than that in Wang's work because CO2 molecules adsorb more strongly on calcite surfaces (this work) than on the quartz walls considered by those authors.

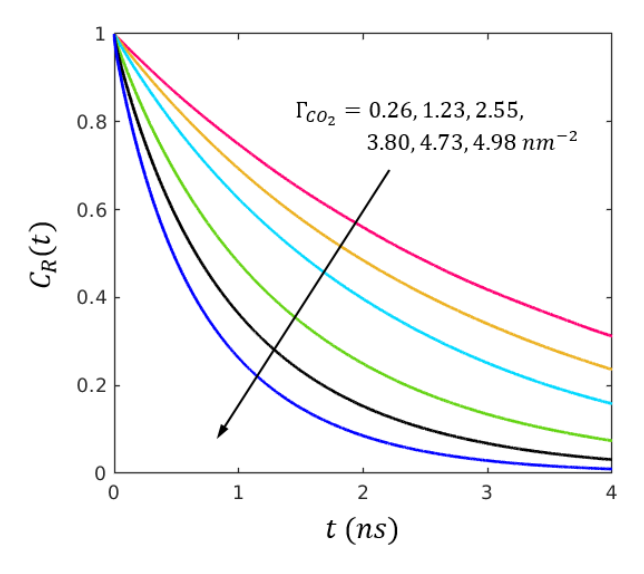


Figure 4. Residence time correlation function of CO₂ molecules adsorbed on a calcite surface exposed to a decane-CO₂ mixture with a pressure of 320 bar.

3.2 Soaking process in single nanopores

In this section, we study the soaking process in a single nanopore connected to a reservoir (see Fig. 1a). As detailed in Section 2, decane is initially trapped in the space at the right side of piston A with a pressure of 280 bar and the CO₂ pressure in the reservoir is 410 bar. At t = 0, the piston A in Fig. 1a is removed to initiate the soaking process.

To gain generalized insight into the dynamics of soaking process using our MD simulations, we nondimensionalize the time using a characteristic time t_c . As we shall see below, soaking is controlled primarily by the diffusion of CO₂ molecules. Therefore, t_c is chosen as

$$t_c = \frac{L_p^2}{D_c} \tag{2}$$

where L_p is the pore length and D_c is the characteristic diffusion coefficient. During the soaking process, the diffusion coefficient of CO₂ molecules varies spatially and temporally. Here, for concreteness, we adopt $D_c = 1.1 \times 10^{-8} \, \text{m}^2/\text{s}$, which is representative of the diffusion coefficients of CO₂ molecules in bulk decane-CO₂ mixture (see Fig. 3a). Therefore, t_c is 79.1 ns.

Basic features. Figure 5 shows the development of decane and CO₂ density distributions during the soaking process. The side view snapshots of the nanopore show that, after piston A is removed, CO₂ molecules are dissolved into the decane and move into the pore's interior. CO₂ molecules not only move in the bulk part of the pore but also move along the pore wall when they become adsorbed. A clear front is observed for the CO₂ molecules adsorbed on pore walls, and this front reaches the end of the pore at $t/t_c \sim 0.39$. Behind this front, a significant fraction of the CO₂ molecules inside the pore is adsorbed on the pore surface. As CO₂ molecules move into the pore, they displace decane molecules from the bulk part of the pore and pore walls concurrently, which leads to decane extraction. These phenomena are qualitatively similar to those visualized by Fang et al.²⁴ These phenomena are easily observed from the evolution of the two-dimensional (2D) density plots of decane and CO₂ molecules along the pore (see Fig. 5b). Figure 5b also shows

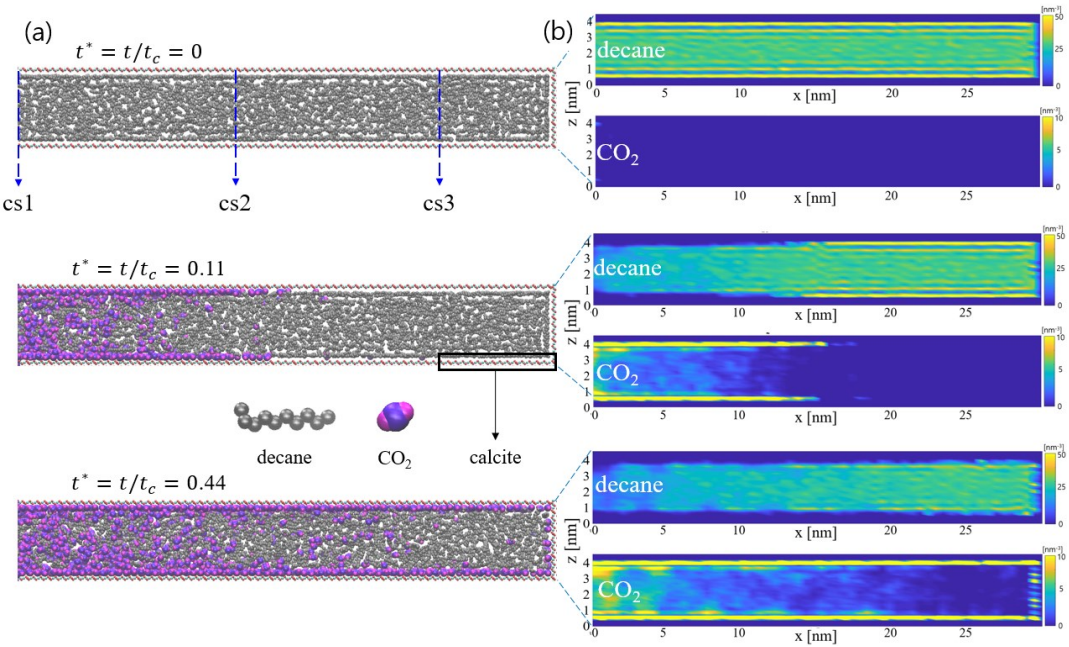


Figure 5. Evolution of decane and CO_2 densities in a calcite slit nanopore during the soaking process. (**a-b**) Side-view snapshots of the nanopore (a) and two-dimensional density distribution of decane and CO_2 in the nanopore at three different times (b). Density distribution is obtained through binning. The bin size in the direction normal to and along the pore (z- and x-directions) is 0.119 nm and 0.492 nm, respectively. Data for a time constant t is the average of the data in the time period [t-50ps, t+50ps] (or [t/t_c-6.3× 10⁻³, t/t_c+6.3× 10⁻³] in dimensionless unit).

that, slightly behind the front of adsorbed CO₂ molecules, the pore wall is nearly saturated by CO₂ while the CO₂ density in the bulk part of the pore remains low.

The rapid increase of adsorbed CO₂ inside the nanopore during soaking and the displacement of decane from pore walls by the adsorbed CO₂ are also clearly observed from the decane and CO₂ density profiles at three representative cross-sections along the pore (denoted as cs1, cs2, and cs3, which correspond to $x/L_p = 0,0.4$, and 0.8, see Fig. 6). At $t/t_c = 0$, a distinct layer of decane molecules exists on pore walls at all three cross-sections, as evident from the high decane density

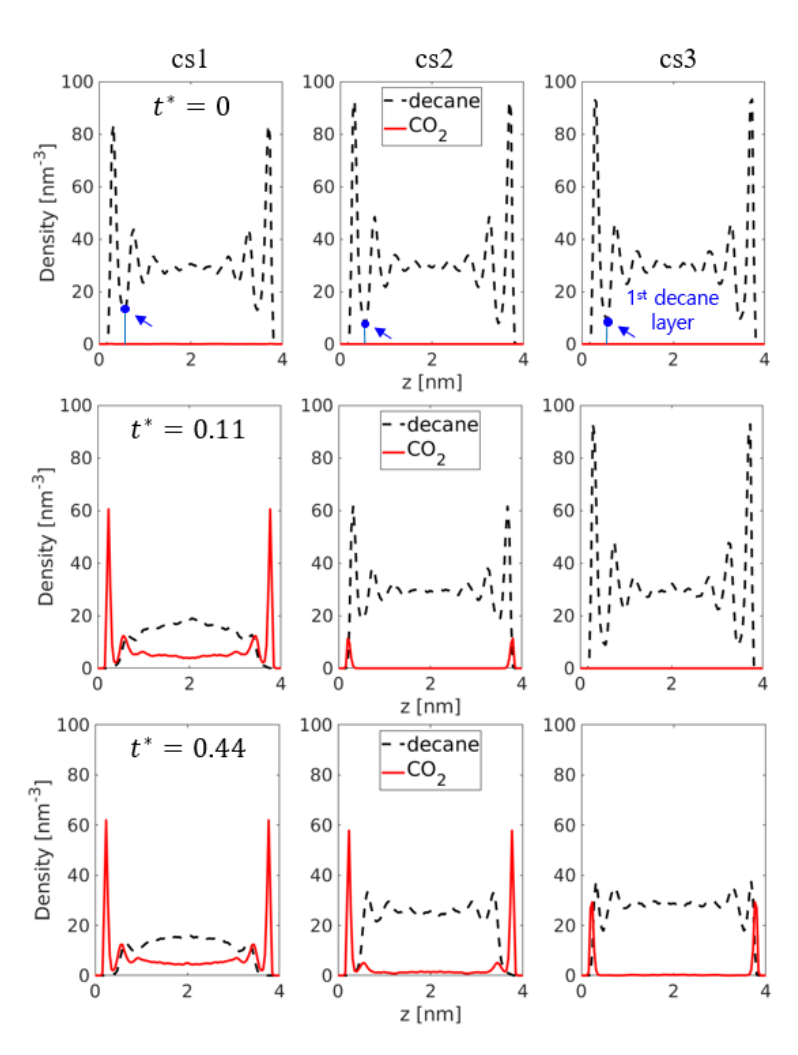


Figure 6. One-dimensional density profiles of decane and CO_2 at three cross-sections along the nanopore (cs1: $x/L_p = 0$, cs2: $x/L_p = 0.4$, and cs3: $x/L_p = 0.8$, see Fig. 5a). The densities of decane and CO_2 are both based on the number of carbon atoms in a unit volume. The first decane layer is formed within 0.555 nm from the calcite pore wall (see the blue arrow at $t^* = 0$).

peak near calcite walls (hereafter, the decane within 0.555 nm from calcite pore walls is termed "adsorbed" decane, while that located further away is termed "free" decane). At $t/t_c = 0.11$, a strong adsorption layer of CO₂ is formed at cs1, the adsorbed decane layer there is fully displaced. While CO₂ molecules also reach cs2, their adsorption on the pore walls is too limited to completely displace the adsorbed decane. At $t/t_c = 0.44$, the adsorbed decane layer at cs2 is fully displaced by the adsorbed CO₂, even though the CO₂ density in the pore's central portion is still very low at this cross-section. Overall, the results in Fig. 5 and Fig. 6 indicate that CO₂ moves into the nanopore both along pore surface and through the central (bulk) region of the pore. This is a major hallmark of the soaking process in nanoscale pores and will be more quantitatively below.

As CO₂ (decane) moves into (out of) the pore, the pressure in the system varies. Figure 7 shows the evolution of the pressure measured on the fixed piston B bounding the decane-CO₂ mixture. The pressure decreases rapidly from ~320 bar to ~220 bar by the end of the simulation. Such a pressure decay is qualitatively similar to that observed in field studies and reservoir simulations. ⁴⁰ Note that these initial and final pressures are lower than the pressure of CO₂ (410 bar) and decane (280 bar) before soaking. The reduction of pressure is caused in part by the mixing of CO₂ with decane and the adsorption of CO₂ on pore walls. The latter reduces the number of free CO₂ inside the pore and the reservoir, and thus causing the fluid pressure in the system to decrease. The finite size of piston A also contributes to the pressure reduction. Specifically, piston A, although made of only one layer of LJ atoms, has a volume of ~12.9 nm³ (The thickness of one-layer LJ atoms is taken as $\sigma = 0.331$ nm (the atom's LJ parameter), and the volume of the atom layer is thus estimated as $\sigma \times L_y \times L_z$ where L_y and L_z are simulation box size in y- and z- directions, respectively). When it is removed to initiate soaking, the volume accessible to decane and CO₂ in the system increases by ~1.7%. Because the compressibility of decane-CO₂ mixture is low, a large

pressure reduction is expected. Eliminating this pressure reduction requires increasing the volume of the pore and reservoir by at least a factor of 10 (and thus computational cost) and thus is not pursued here.

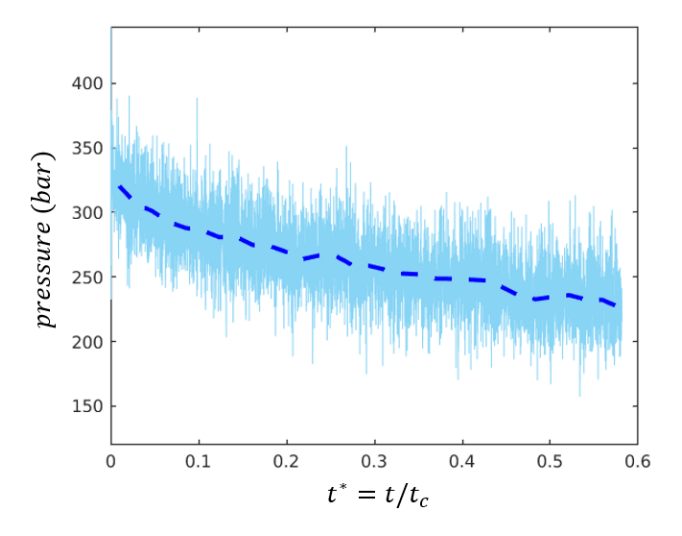


Figure 7. Evolution of the pressure on piston B bounding the decane-CO₂ mixture in Fig. 1a. The blue dashed line is a running average of the pressure with a window size of $0.019t_c$

CO₂ accumulation and decane depletion statistics. The accumulation of CO₂ molecules in the nanopore (N_{co2}) and its contributions by free and adsorbed CO₂ molecules ($N_{co2,f}$ and $N_{co2,ad}$) are determined from the trajectories and shown in Figure 8. The accumulation rates of adsorbed and free CO₂ molecules are similar and decrease with time (see Fig. S4a in the Supplementary Material). At very short time ($t/t_c \leq 0.01$), the pressure imbalance between the reservoir and pore causes a CO₂ flow into the pore and a linear increase of CO₂ inside the pore (see Section S3 and Fig. S5 in the Supplementary Material). At slightly larger time, which is the focus of this work, a pressure equilibration is established and diffusion becomes important. In fact, we find that the accumulation of both free and adsorbed CO₂ obeys a diffusive scaling law. Specifically, before the front of adsorbed CO₂ molecules reaches the pore's end at $t/t_c \sim 0.39$, both $N_{co2,ad}^2$ and $N_{co2,f}^2$ increases linearly with time (see Fig. 8a). At $t/t_c \sim 0.39$, adsorbed CO₂ molecules account for 55.1% of the CO₂ molecules inside the pore.

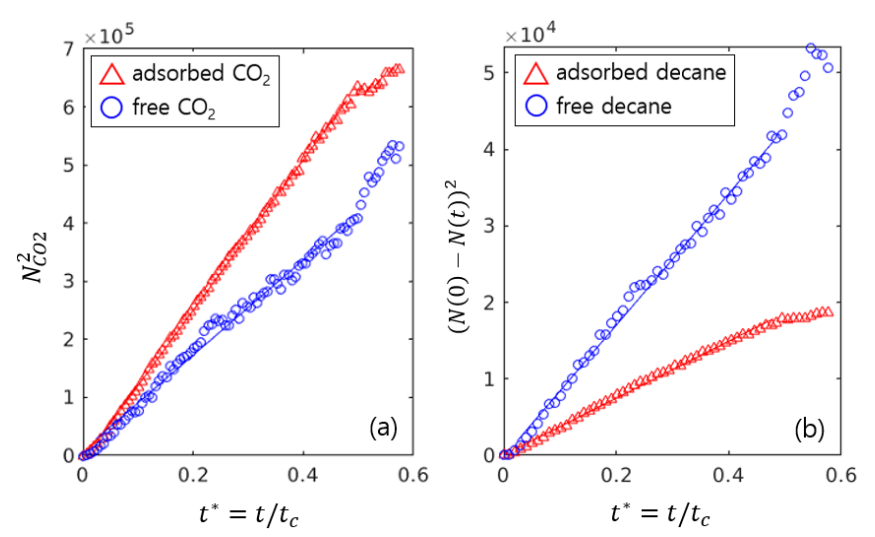


Figure 8. (a) The evolution of the number of CO₂ molecules in the nanopore and its contributions by adsorbed and free CO₂ molecules. (b) The evolution of the number of decane molecules in the nanopore. A CO₂ molecule is considered as "adsorbed" ("free") if its distance to the nearest pore wall is less (larger) than 0.398 nm. An atom of a decane molecule is considered as "adsorbed" ("free") if its distance to the nearest pore wall is smaller (larger) than 0.555 nm.

The depletion of decane from the nanopore is quantified by tracking the number of decane molecules N_{c10} , the adsorbed decane molecules $(N_{c10,ad})$, and free decane molecule $(N_{c10,f})$ in the nanopore. The removal rate of both adsorbed and free decane decreases with time, and within the time studied here, the amount of adsorbed decane removed from the pore is 62% of the amount of free decane removed (see Fig. S4b in the Supplementary Material). Similar to the transport of CO₂ into the nanopore, the removal of decane follows a diffusive scaling law: except at very early time and after the front of adsorbed CO₂ reaches the pore's end, both $\left(N_{c10,ad}(0) - N_{c10,ad}(t)\right)^2$ and $\left(N_{c10,f}(0) - N_{c10,f}(t)\right)^2$ increase linearly with time (see Fig. 8b).

Before the front of the adsorbed CO₂ reaches the end of the nanopore, the accumulation of CO₂ inside the nanopore follows the diffusive scaling law. Hence, the transport of CO₂ in the nanopore during the soaking process can be treated as a diffusion. Such a diffusion process is coupled tightly with that of decane and can only be described rigorously using multi-component transport theories. Nevertheless, we can extract an effective diffusion coefficient of CO₂ ingression by analyzing the

movement of the diffusion fronts of the adsorbed and free CO₂ molecules inside the pore. To this end, we compute the one-dimensional (1D) density profiles of adsorbed and free CO₂ along the pore, $\Gamma_{co2}(x)$ and $\bar{\rho}_{co2,f}(x)$ using $\Gamma_{co2}(x) = \int_0^{\delta} \rho_{co2}(x,z) dz$ and $\bar{\rho}_{co2,f}(x) = \int_{\delta}^{w-\delta} \rho_{co2}(x,z) dz/(w-2\delta)$, where $\delta = 0.398$ nm is the thickness of CO₂ adsorption layer and w is the pore width.

Figure 9a and 9b shows the evolution of $\Gamma_{co2}(x)$ and $\bar{\rho}_{co2,f}(x)$ profiles during the soaking process. We observe that, $\bar{\rho}_{co2,f}(x)$ decreases smoothly from the pore's entrance to its interior. $\bar{\rho}_{co2,f}(x)$ exhibits a concaved shape and its front spreads with increasing time, similar to those observed in mass diffusion along a 1D pore or through a semi-infinite domain. $\Gamma_{co2}(x)$, however, exhibits an inverse S-shape. In particular, as the distance from the pore entrance increases, a mildly decrease is first observed, followed by a sharp drop. Such a profile can be understood as follows. Because the adsorbed and free CO₂ molecules can exchange at a nanosecond time scale (see Fig. 4), they are at quasi-local equilibrium at each cross-section along the nanopore during the soaking process. Since Γ_{co2} approaches its saturation value at rather low free CO₂ density and increases slowly at $\rho_{co2}^b > 0.5$ nm⁻³ (see Fig. 2b), Γ_{co2} is close to saturation and varies slowly near the pore entrance, and Γ_{co2} only drops sharply near the front of the free CO₂ density profile, where CO₂ density is low.

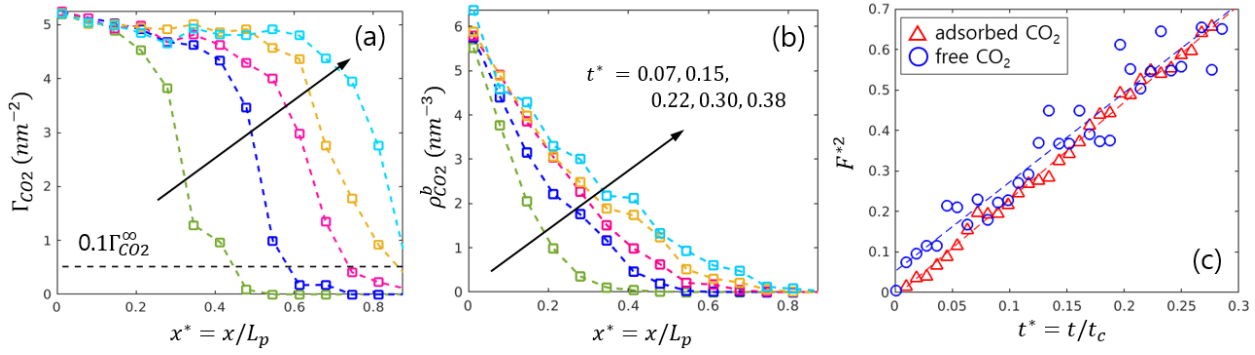


Figure 9. (a-b) Evolution of the one-dimensional density of adsorbed CO₂ molecules (a) and free CO₂ molecules (b) along pore length direction during the soaking process. (c) Evolution of the diffusion front of surface and free CO₂ during the soaking process.

From the temporal evolution of $\Gamma_{co2}(x)$ and $\bar{\rho}_{co2,f}(x)$, we extract the dynamics of the diffusion front of free and adsorbed CO₂. Specifically, at any given time, the diffusion front of adsorbed CO₂, $F_{ad}(t)$, is taken as the position where $\Gamma_{co2}(x)$ reaches a threshold value of $0.1\Gamma_{co2}^{\infty}$. The diffusion front of the free CO₂, $F_f(t)$, is taken as the position where $\bar{\rho}_{co2,f}(x)$ reaches 0.0133 nm⁻³, at which $\Gamma_{co2}=0.1\Gamma_{co2}^{\infty}$ according to the CO₂ adsorption isotherm in Fig. 2b. Figure 9c shows that the movement of the diffusion front of both free and adsorbed CO₂ follows the square root scaling law, consistent with the diffusive nature of CO₂ accumulation in nanopore revealed by Fig. 8a. Therefore, although the transport of CO₂ during the soaking process is complicated by physics such as the coupling of the transport of CO₂ and decane, it can be described phenomenologically by a diffusion equation with an effective diffusion coefficient. By using linear regression of $F_{ad}(t)^2$ and $F_f(t)^2$ at time before the diffusion fronts of free and adsorbed CO₂ reach the pore's end and the analytical solution for 1D transient diffusion in a semi-infinite domain, the effective diffusion coefficients for the movement of adsorbed and free CO2's diffusion fronts are extracted as 4.62×10^{-9} and 4.49×10^{-9} m²/s, respectively (see Section S3 in Supplementary Material for details). These effective diffusion coefficients are close to each other because the transports of adsorbed and free CO₂ along the pore are tightly coupled due to the rapid exchange between them (see Fig. 4). These effective diffusion coefficients are smaller than the self-diffusion coefficient of free CO2 in bulk decane-CO2 mixtures shown in Fig. 3a. Two factors mainly cause this observation. First, the net transport of CO₂ along the pore length is contributed partly by the CO₂ adsorbed on the pore walls, which has a lower diffusion coefficient (3.3-9×10⁻⁹ m²/s, see Fig. 3b). Second, the transport of CO₂ molecules into the pore's interior is hindered by their interactions with the decane molecules leaving the pore.

357

358

359

360

361

362

363

364

365

366

367

368

369

370

371

372

373

374

375

376

377

378

379

Importance of adsorption in overall CO₂ storage and transport. The above results show

that the adsorption of CO_2 molecules on the pore surface and their transport along the pore surface strongly affect the utilization and storage of CO_2 inside nanopore during the soaking. To gauge the importance of surface adsorption relative to volumetric absorption in a pore with a width w, we introduce a surface storage factor S_{ad} :

384
$$S_{ad} = \frac{2 \times \Gamma_{CO_2}}{\rho_{CO_2}^b \times (w - 2\delta)}$$
 (3)

Here, we assume that a pore can be divided into two zones: the CO₂ adsorption zone within δ from pore walls and the bulk zone in which the density of CO₂ is $\rho_{CO_2}^b$ (for calcite surfaces, δ = 0.398 nm). This assumption is reasonable for pores with w " 2δ because CO₂ density is approximately constant outside the CO₂ adsorption layer (see Fig. 2a). At equilibrium, Γ_{CO_2} is related to the CO₂ density in the bulk zone $\rho_{CO_2}^b$ through the CO₂ adsorption isotherm. Using the isotherm in Fig. 2b, the surface storage factor is estimated for slit calcite pores with various widths. Figure 10 shows that, in 4.0 nm-wide pores, surface adsorption contributes more to CO₂ storage than volumetric absorption when the bulk CO₂ density is smaller than a threshold of ~3.60 nm⁻³. At a given CO₂ bulk density $\rho_{CO_2}^b$, the surface storage factor increases as the pore width decreases, e.g., at $\rho_{CO_2}^b = 3.3$ nm⁻³, which corresponds to the CO₂ density in a bulk decane-CO₂ mixture at 100 bar and 344.5 K, ²⁶ S_{ad} is estimated to be 0.261 for w = 15 nm and 1.682 for w = 3.0 nm. Clearly, surface adsorption contributes greatly to the net CO₂ storage in narrow pores or when bulk CO₂ density is low.

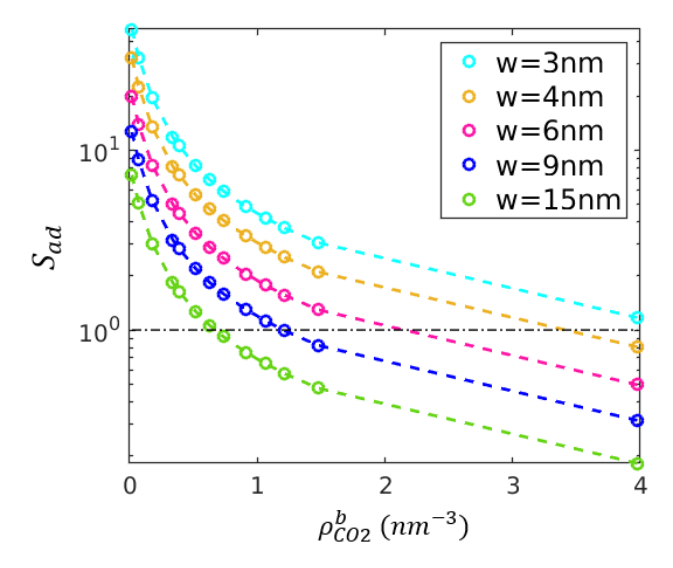


Figure 10. The variation of CO₂ surface storage factor with CO₂ bulk density in different nanopores.

During the soaking process, CO₂ is transported into a pore's interior mostly in two modes: the diffusion of free CO₂ in the pore's bulk zone and the diffusion of adsorbed CO₂ on pore walls. Due to the relatively rapid exchange between free and adsorbed CO₂, these two modes are coupled, and they are further coupled with the transport of decane out of the pore. To gauge the importance of surface diffusion relative to bulk diffusion qualitatively, we introduce a surface diffusion factor κ_s as the ratio of the surface and bulk diffusion fluxes. In the absence of reliable and simple theories for the transport of CO₂-decane mixture confined in nanopores, *as a first approximation*, Fick's law is used to describe these diffusion fluxes. Thus κ_s can be written as

$$\kappa_{S} = \frac{-2D_{S} \frac{\partial \Gamma_{CO2}}{\partial x}}{-D_{b}(w-2\delta) \frac{\partial \rho_{CO2}^{b}}{\partial x}} = \frac{2D_{S}}{D_{b}(w-2\delta)} \frac{\partial \Gamma_{CO2}}{\partial \rho_{CO2}^{b}}$$

$$(4)$$

where D_s (D_b) is the diffusion coefficient of adsorbed (free) CO₂ shown in Fig. 3. To compute κ_s , we fit the CO₂ adsorption isotherm in Fig. 2b to the Langmuir isotherm $\Gamma_{CO_2} = \Gamma_{co2}^{\infty} \frac{\rho_{co2}^b}{\rho_{co2}^b + a}$ (see Fig. S6 in the Supplementary Material) and evaluate $\partial \Gamma_{co2}/\partial \rho_{co2}^b$ analytically. Figure 11 shows the variation of κ_s in calcite nanopores as a function of the bulk CO₂ density in a 4 nm-wide

calcite pores. Surface diffusion is stronger than bulk diffusion if $\rho_{co2}^b < 0.046$ nm⁻³ (or equivalently, $\Gamma_{co2} < 1.75$ nm⁻²), but becomes less than 10% bulk diffusion as ρ_{co2}^b increases beyond 0.198 nm⁻³ and CO₂ adsorption density reaches 0.78 $\Gamma_{CO_2}^\infty$. We conclude that when CO₂ adsorption approaches saturation, the overall CO₂ transport is dominated by bulk diffusion; in the opposite limit, surface diffusion dominates. During the soaking process, CO₂ adsorption on pore walls varies from zero in front of the CO₂ diffusion front to near saturation (Γ_{CO2}^∞) at positions far behind the CO₂ diffusion front. Therefore, surface and bulk diffusion can be important in different regions along one nanopore, and the region in which surface or bulk diffusion dominates is not fixed but changes as the CO₂ diffusion front moves.

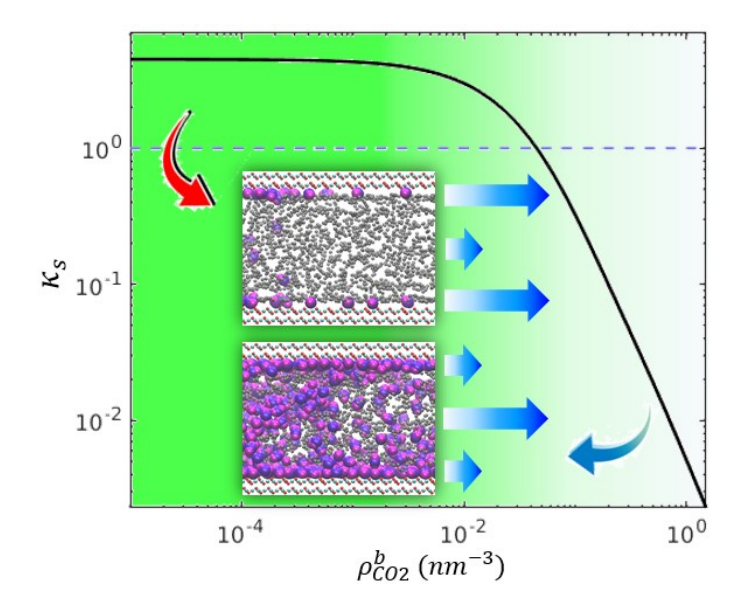


Figure 11. Variation of the surface diffusion factor in calcite nanopores as a function of bulk CO₂ density.

4. Conclusions

In summary, we study the soaking step of CO₂ Huff-n-Puff in unconventional oil reservoirs at the single-nanopore scale using molecular simulations. Because of the strong interactions between CO₂ and calcite pore walls, except at the very early stage, CO₂ is transported deep into the 4 nmwide calcite pore adopted here through two pathways: the surface diffusion of adsorbed CO₂ and bulk diffusion of free CO₂. These pathways are coupled by the nanosecond scale exchange between the adsorbed and free CO₂. During soaking, the accumulation of adsorbed and free CO₂ in the nanopore occurs at similar rates and follows the diffusive scaling law before the diffusion front of CO₂ reaches the pore's end. The effective diffusion coefficient of the CO₂ diffusion front is ~50% smaller than the diffusion coefficient of bulk CO₂.

Existing models of CO₂ Huff-n-Puff in unconventional oil reservoirs typically do not explicitly consider the adsorption of CO₂ molecules on pore walls and their surface diffusion. Our results, however, show that these effects can play a major role in the overall storage and transport of CO₂ in narrow pores. The importance of these effects can be qualitatively assessed using the surface storage factors and surface transport factors introduced here.

Supplementary Material: Force field parameters, adsorption and dynamics of CO₂ molecules on calcite surfaces, evolution of the amount of CO₂ and decane molecules inside nanopores during soaking, effective diffusion coefficient for the movement of diffusion fronts of free and adsorbed CO₂, fitting of the CO₂ adsorption isotherm to the Langmuir isotherm model.

Acknowledgments

We thank the ARC at Virginia Tech for generous allocations of computer time. The work at Virginia Tech is partially supported by the NSF under grant number CBET-1705287.

References

- 1. U.S. Energy Information Administration, Annual Energy Outlook 2017; 2017.
- 2. Nelson, P. H., Pore-throat sizes in sandstones, tight sandstones, and shales. AAPG bulletin
- **2009,** *93* (3), 329-340.

- 451 3. Abedini, A.; Torabi, F., On the CO2 storage potential of cyclic CO2 injection process for
- 452 enhanced oil recovery. Fuel **2014**, 124, 14-27.
- 453 4. Zhou, X.; Yuan, Q. W.; Peng, X. L.; Zeng, F. H.; Zhang, L. H., A critical review of the
- 454 CO2 huff 'n' puff process for enhanced heavy oil recovery. Fuel **2018**, 215, 813-824.
- 5. Tharanivasan, A. K.; Yang, C.; Gu, Y., Measurements of molecular diffusion coefficients of
- 456 carbon dioxide, methane, and propane in heavy oil under reservoir conditions. *Energy & fuels* **2006**,
- 457 *20* (6), 2509-2517.
- 458 6. Sorensen, J. A.; Hamling, J. A., Historical bakken test data provide critical insights on EOR
- in tight oil plays,. *The American Oil & Gas Reporter* 2016, pp 55-61.
- 7. Rassenfoss, S., Shale EOR Works, But Will It Make a Difference? Journal of Petroleum
- 461 *Technology* **2017**, *69* (10), 34-40.
- 8. Sheng, J. J., Enhanced oil recovery in shale reservoirs by gas injection. *Journal of Natural*
- 463 *Gas Science and Engineering* **2015**, *22*, 252-259.
- 9. Sheng, J. J., Critical review of field EOR projects in shale and tight reservoirs. *Journal of*
- 465 Petroleum Science and Engineering 2017, 159, 654-665.
- 10. Todd, H. B.; Evans, J. G. In *Improved oil recovery IOR pilot projects in the Bakken formation*,
- SPE low perm symposium, Society of Petroleum Engineers: 2016; pp SPE-180270-MS.
- 11. Chen, C.; Gu, M., Investigation of cyclic CO2 huff-and-puff recovery in shale oil reservoirs
- using reservoir simulation and sensitivity analysis. Fuel **2017**, 188, 102-111.
- 470 12. Simpson, M. R., The CO2 huff'n'puff process in a bottomwater-drive reservoir. *Journal of*
- 471 *petroleum technology* **1988,** *40* (07), 887-893.
- 13. Maneeintr, K.; Babadagli, T.; Sasaki, K.; Sugai, Y., Analysis of heavy oil emulsion-carbon
- dioxide system on oil-swelling factor and interfacial tension by using pendant drop method for

- 474 enhanced oil recovery and carbon dioxide storage. *International Journal of Environmental Science*
- *and Development* **2014**, *5* (2), 118-123.
- 476 14. Mangalsingh, D.; Jagai, T. In A laboratory investigation of the carbon dioxide immiscible
- 477 process, SPE Latin America/Caribbean Petroleum Engineering Conference, Society of Petroleum
- 478 Engineers: 1996.
- 479 15. Khatib, A. K.; Earlougher, R.; Kantar, K. In CO2 injection as an immiscible application for
- 480 enhanced recovery in heavy oil reservoirs, SPE California Regional Meeting, Society of Petroleum
- 481 Engineers: 1981.
- 482 16. Chen, C.; Balhoff, M. T.; Mohanty, K. K., Effect of reservoir heterogeneity on primary
- recovery and CO2 huff'n'puff recovery in shale-oil reservoirs. SPE Reservoir Evaluation &
- 484 Engineering **2014**, 17 (03), 404-413.
- 485 17. Patton, J. T.; Coats, K. H.; Spence, K., Carbon Dioxide well stimulation: Part 1-A parametric
- 486 study. *Journal of Petroleum Technology* **1982,** *34* (08), 1798-1804.
- 487 18. Liu, X.; Zhang, D., A review of phase behavior simulation of hydrocarbons in confined space:
- 488 Implications for shale oil and shale gas. Journal of Natural Gas Science and Engineering 2019,
- 489 *68*, 102901.
- 490 19. Ghasemi, M.; Astutik, W.; Alavian, S. A.; Whitson, C. H.; Sigalas, L.; Olsen, D.;
- 491 Suicmez, V. S., Determining diffusion coefficients for carbon dioxide injection in oil-saturated
- chalk by use of a constant-volume-diffusion method. SPE Journal 2017, 22 (02), 505-520.
- 493 20. Yuan, Q.; Zhou, X.; Zeng, F.; Knorr, K. D.; Imran, M. In Effects of concentration-
- 494 dependent diffusion on mass transfer and frontal instability in solvent-based processes, SPE
- 495 Canada Heavy Oil Technical Conference, Society of Petroleum Engineers: 2017.
- 496 21. Zhao, Y.; Jin, Z., Hydrocarbon mixture phase behavior in multi-scale systems in relation to

- shale oil recovery: The effect of pore size distributions. *Fuel* **2021**, *291*, 120141.
- 498 22. Fang, T.; Zhang, Y.; Yan, Y.; Wang, Z.; Zhang, J., Molecular insight into the oil
- 499 extraction and transport in CO2 flooding with reservoir depressurization. *International Journal of*
- 500 *Heat and Mass Transfer* **2020,** *148*, 119051.
- 501 23. Fang, T.; Zhang, Y.; Ding, B.; Yan, Y.; Zhang, J., Static and dynamic behavior of CO2
- enhanced oil recovery in nanoslits: Effects of mineral type and oil components. *International*
- 503 *Journal of Heat and Mass Transfer* **2020,** *153*, 119583.
- 504 24. Fang, T.; Zhang, Y.; Ma, R.; Yan, Y.; Dai, C.; Zhang, J., Oil extraction mechanism in
- 505 CO2 flooding from rough surface: Molecular dynamics simulation. *Applied Surface Science* **2019**,
- 506 *494*, 80-86.
- 507 25. Peng, F.; Xiong, K.; Wang, R.; Li, Y.; Guo, Z.; Feng, G., Molecular Insight into
- Microbehaviors of n-Decane and CO2 in Mineral Nanopores. Energy & Fuels 2020, 34 (3), 2925-
- 509 2935.
- 510 26. Wang, R.; Peng, F.; Song, K.; Feng, G.; Guo, Z., Molecular dynamics study of
- interfacial properties in CO2 enhanced oil recovery. Fluid Phase Equilibria 2018, 467, 25-32.
- 512 27. Santos, M. S.; Franco, L. F. M.; Castier, M.; Economou, I. G., Molecular Dynamics
- 513 Simulation of n-Alkanes and CO2 Confined by Calcite Nanopores. *Energy & Fuels* **2018**, *32* (2),
- 514 1934-1941.
- 515 28. Moh, D. Y.; Fang, C.; Yin, X.; Qiao, R., Interfacial CO2-mediated nanoscale oil transport:
- from impediment to enhancement. Physical Chemistry Chemical Physics 2020, 22 (40), 23057-
- 517 23063.
- 518 29. Zhang, W.; Feng, Q.; Wang, S.; Xing, X.; Jin, Z., CO2-regulated octane flow in calcite
- nanopores from molecular perspectives. *Fuel* **2021**, *286*, 119299.

- 520 30. Wang, S.; Javadpour, F.; Feng, Q., Fast mass transport of oil and supercritical carbon dioxide
- through organic nanopores in shale. *Fuel* **2016**, *181*, 741-758.
- 31. Takbiri-Borujeni, A.; Kazemi, M.; Liu, S.; Zhong, Z., Molecular simulation of enhanced
- oil recovery in shale. *Energy Procedia* **2019**, *158*, 6067-6072.
- 32. Zhu, Z.; Fang, C.; Qiao, R.; Yin, X.; Ozkan, E., Experimental and Molecular Insights
- on Mitigation of Hydrocarbon Sieving in Niobrara Shale by CO2 Huff 'n' Puff. SPE Journal 2020,
- 526 SPE-196136-PA, DOI:10.2118/196136-PA.
- 33. Kamruzzaman, A.; Prasad, M.; Sonnenberg, S., Petrophysical rock typing in unconventional
- shale plays: The Niobrara Formation case study. *Interpretation* **2019**, 7 (4), SJ7-SJ22.
- 529 34. Song, Z.; Li, Y.; Song, Y.; Bai, B.; Hou, J.; Song, K.; Jiang, A.; Su, S. In *A critical*
- 530 review of CO2 enhanced oil recovery in tight oil reservoirs of North America and China,
- 531 SPE/IATMI Asia Pacific Oil & gas conference and exhibition, OnePetro: 2020.
- 35. Martínez, L.; Andrade, R.; Birgin, E. G.; Martínez, J. M., PACKMOL: a package for
- building initial configurations for molecular dynamics simulations. Journal of computational
- *chemistry* **2009**, *30* (13), 2157-2164.
- 36. Rahaman, A.; Grassian, V. H.; Margulis, C. J., Dynamics of water adsorption onto a calcite
- surface as a function of relative humidity. The Journal of Physical Chemistry C 2008, 112 (6),
- 537 2109-2115.
- 538 37. Nath, S. K.; Escobedo, F. A.; de Pablo, J. J., On the simulation of vapor-liquid equilibria
- for alkanes. *The Journal of chemical physics* **1998**, *108* (23), 9905-9911.
- 38. Aimei, Z.; Zhang, X.; Qinglin, L.; Zhang, Q., A fully flexible potential model for carbon
- dioxide. Chinese Journal of Chemical Engineering 2009, 17 (2), 268-272.
- 39. Martin, M. G.; Siepmann, J. I., Transferable potentials for phase equilibria. 1. United-atom

- description of n-alkanes. The Journal of Physical Chemistry B 1998, 102 (14), 2569-2577.
- 544 40. Iino, A.; Onishi, T.; Datta-Gupta, A., Optimizing CO2- and Field-Gas-Injection EOR in
- 545 Unconventional Reservoirs Using the Fast-Marching Method. SPE Reservoir Evaluation &
- 546 Engineering **2020**, 23 (01), 261-281.
- 547 41. Bergman, T. L.; Incropera, F. P.; DeWitt, D. P.; Lavine, A. S., Fundamentals of heat and
- 548 *mass transfer*. John Wiley & Sons: 2011.